CrossMark

J. Fluid Mech. (2018), *vol.* 848, *pp.* 545–559. © Cambridge University Press 2018. This is a work of the U.S. Government and is not subject to copyright protection in the United States.
doi:10.1017/jfm.2018.366

Frequency–wavenumber spectral analysis of spatio-temporal flows

Christopher J. Geoga[1,†], Charlotte L. Haley[1], Andrew R. Siegel[1,2] and Mihai Anitescu[1,3]

[1]Argonne National Laboratory, Mathematics and Computer Science Division, 9700 S. Cass Ave., Lemont, IL 60439, USA

[2]University of Chicago, Department of Computer Science, 1100 E. 58th Street, Chicago, IL 60637, USA

[3]University of Chicago, Department of Statistics, George Herbert Jones Laboratory 5747 S. Ellis Ave., Chicago, IL 60637, USA

(Received 11 December 2017; revised 5 March 2018; accepted 26 April 2018; first published online 8 June 2018)

We propose a fully spatio-temporal approach for identifying spatially varying modes of oscillation in fluid dynamics simulation output by means of multitaper frequency–wavenumber spectral analysis. One-dimensional spectrum estimation has proven to be a valuable tool in the analysis of turbulence data applied spatially to determine the rate of energy transport between spatial scales, or temporally to determine frequencies of oscillatory flows. It also allows for the quantitative comparison of flow characteristics between two scenarios using a standard basis. It has the limitation, however, that it neglects coupling between spatial and temporal structures. Two-dimensional frequency–wavenumber spectral analysis allows one to decompose waveforms into standing or travelling variety. The extended higher-dimensional multitaper method proposed here is shown to have improved statistical properties over conventional non-parametric spectral estimators, and is accompanied by confidence intervals which estimate their uncertainty. Multitaper frequency–wavenumber analysis is applied to a canonical benchmark problem, namely, a direct numerical simulation of von Kármán vortex shedding off a square wall-mounted cylinder with two inflow scenarios with matching momentum-thickness Reynolds numbers $Re_\theta \approx 1000$ at the obstacle. Frequency–wavenumber analysis of a two-dimensional section of these data reveals that although both the laminar and turbulent inflow scenarios show a turbulent $-5/3$ cascade in wavenumber (ν) and frequency (f), the flow characteristics differ in that there is a significantly more prominent discrete harmonic oscillation near $(f, \nu) = (0.2, 0.21)$ in wavenumber and frequency in the laminar inflow scenario than the turbulent scenario. This frequency–wavenumber pair corresponds to a travelling wave with velocity near one near the centre path of the vortex street.

Key words: mathematical foundations, vortex flows, vortex streets

† Email address for correspondence: cgeoga@anl.gov

https://doi.org/10.1017/jfm.2018.366 Published online by Cambridge University Press

1. Introduction

Spatio-temporal flow structures are often analysed by separately examining either spatial or temporal aspects of the flow. The spatial flow structures can be summarized by using modal decompositions, such as proper orthogonal decomposition (POD) (Berkooz, Holmes & Lumley 1993), dynamic mode decomposition (DMD) for nonlinear flows (Holmes, Lumley & Berkooz 1998), balancing modes for linear systems (Rowley 2005; Schmidt *et al.* 2017) or spectral analysis of the Koopman operator (Rowley *et al.* 2009). Analysis of time histories for oscillatory structures is often done by using Fourier decompositions of the series at a particular subjectively chosen gridpoint in the simulation geometry. Univariate spectral analysis does not, however, give information about frequency–wavenumber coupling between oscillatory structures in spatially inhomogeneous flow. For this, one must use a higher-dimensional technique that is agnostic to the choice of spatial location, and incorporates directional spatial information.

Frequency–wavenumber spectral analysis (Hayashi 1979; von Storch & Zwiers 1999; Cressie & Wikle 2011) originated in the atmospheric physics literature and can be used to partition waves into standing and travelling variety, the major advantage of which is the extraction of velocities of the travelling waves. The multitaper method for two-dimensional spectrum analysis (Thomson 1982) has been described by Hanssen (1997), the problem of simultaneously strictly limiting the spatial duration, concentrating the spectral mass of signals both in Cartesian space and on the sphere has been described by Slepian (1964), and the application to geophysical problems has been presented by Simons & Wang (2011), Kirby (2014). Although multidimensional optimally concentrated two-dimensional (2-D) Cartesian tapers have been suggested for spectrum analysis, this is the first practical implementation of such a scheme. Here we show that multitaper frequency–wavenumber spectra have improved statistical properties over frequency–wavenumber periodograms. Further, they provide a natural method for computing confidence intervals by using a bootstrapping technique (Thomson & Chave 1991) to study the uncertainty of point estimates.

We apply two-dimensional multitaper frequency–wavenumber analysis to the quantitative comparison of flow structures in two different scenarios for a classic benchmark problem, separating flows into standing and travelling wave type. Vinuesa *et al.* (2015) used direct numerical simulation (DNS) to study the flow around a wall-mounted square cylinder with turbulent and laminar inflow. The effect of inflow conditions was assessed by considering two different cases with matching momentum-thickness Reynolds numbers $Re_\theta \approx 1000$ at the obstacle: the first case was a fully turbulent zero-pressure-gradient boundary layer, and the second was a laminar boundary layer with prescribed Blasius inflow profile farther upstream. The authors reported differing boundary layer characteristics ahead of the cylinder in the two regimes, as well as wider width of the wake in the turbulent regime. The main vortex shedding frequency in the von Kármán street was determined to be $St \approx 0.1$ in both inflow cases (Vinuesa *et al.* 2015, figure 17). We complete a full frequency–wavenumber spectral analysis on a section of these data composed of one spatial dimension and one time dimension, identifying both the frequency and wavenumber of oscillation of the dominant waveforms, in order to deduce the velocity of the von Kármán vortices shedding in the wake of the obstacle and to compare the two spectra for artefacts having this velocity.

https://doi.org/10.1017/jfm.2018.366 Published online by Cambridge University Press

2. Frequency–wavenumber spectral analysis

The wavenumber–frequency spectrum reveals dynamic features of spatio-temporal processes such as travelling oscillatory components and turbulent energy cascades. Initially introduced in the atmospheric physics literature by Pratt (1976), Hayashi (1979), it is useful for determining large-scale properties of atmospheric flows such as velocities of Rossby waves.

2.1. *Multitaper spectral analysis*

Beginning with a zero-mean stationary spatio-temporal process $x(t, s)$, where $t = 0, \ldots, N_t - 1$ is a temporal index and $s = 0, \ldots, N_s - 1$ is a one-dimensional spatial index, with unit sampling temporally and spatially, the frequency–wavenumber multitaper spectrum estimator is defined by first multiplying the data pointwise by a set of J two-dimensional discrete tapers, $v^{(j)}(t, s)$, $j = 0, \ldots, J - 1$, to be defined in § 2.2 (see note on the non-trivial nature of demeaning spatio-temporal processes for spectrum analysis in supplementary section appendix A). Applying the Fourier transform along the spatial dimension gives

$$y^{(j)}(t, \nu) = \sum_{s=0}^{N_s-1} v^{(j)}(t, s)x(t, s)\mathrm{e}^{-2\pi \mathrm{i}\nu s}, \tag{2.1}$$

where $\nu = 0, \ldots, 1/2$ is the wavenumber or reciprocal of the wavelength in cycles per unit length. Proceeding in the spirit of von Storch & Zwiers (1999), Cressie & Wikle (2011), one then extracts the real and imaginary parts of $y^{(j)}$, given as

$$a^{(j)}(t, \nu) = y^{(j)}(t, \nu) + y^{(j)}(t, -\nu), \tag{2.2}$$

$$b^{(j)}(t, \nu) = y^{(j)}(t, -\nu) - y^{(j)}(t, \nu), \tag{2.3}$$

respectively. We denote the temporal spectra of $a^{(j)}(t, \nu)$ and $b^{(j)}(t, \nu)$ as $\widehat{S}_a^{(j)}(f, \nu)$ and $\widehat{S}_b^{(j)}(f, \nu)$, with cross-spectrum $\widehat{S}_{a,b}^{(j)}(f, \nu)$, i.e.

$$\widehat{S}_a(f, \nu) = \frac{1}{J}\sum_{j=0}^{J-1}\left|\sum_{t=0}^{N_t-1} a^{(j)}(t, \nu)\mathrm{e}^{-\mathrm{i}2\pi ft}\right|^2, \tag{2.4}$$

$$\widehat{S}_{a,b}(f, \nu) = \frac{1}{J}\sum_{j=0}^{J-1}\sum_{t_1=0}^{N_t-1}\sum_{t_2=0}^{N_t-1} a^{(j)}(t_1, \nu)b^{(j)}(t_2, \nu)\mathrm{e}^{-\mathrm{i}2\pi f(t_1-t_2)}, \tag{2.5}$$

where the real (in-phase) part of the cross-spectrum estimate; $\widehat{S}_{a,b}(f, \nu)$ is the cospectrum, denoted $\widehat{c}_{a,b}(f, \nu)$; and the imaginary part is the quadrature spectrum, denoted $\widehat{q}_{a,b}(f, \nu)$. The total spectrum estimate, simply computed as the average of the J spectrum estimates

$$z^{(j)}(f, \nu) = \sum_{m=0}^{N_t-1} y^{(j)}(t, \nu)\mathrm{e}^{-\mathrm{i}2\pi ft}; \tag{2.6}$$

$$\widehat{S}^{(j)}(f, \nu) = |z^{(j)}(f, \nu)|^2; \quad \widehat{S}(f, \nu) = \frac{1}{J}\sum_{j=0}^{J-1}\widehat{S^{(j)}}(f, \nu) \tag{2.7a,b}$$

https://doi.org/10.1017/jfm.2018.366 Published online by Cambridge University Press

can be decomposed into standing and travelling components by combining individual spectra with the quadrature spectrum and cospectrum. Standing waves travel coherently with the same magnitude and opposite phase. Define the (symmetric) standing wavenumber–frequency spectrum as

$$S_S(f,\nu) = \left\{ \tfrac{1}{4}[\widehat{S}_a(f,\nu) - \widehat{S}_b(f,\nu)]^2 + \widehat{c}^2_{a,b}(f,\nu) \right\}^{1/2}. \tag{2.8}$$

The cospectrum is large when two waves are travelling near 90° out of phase; but since the sine and cosine Fourier coefficients are already 90° out of phase, a peak is produced in the quadrature spectrum $\widehat{q}_{a,b}(f,\nu)$ at wavenumber ν and frequency f when a travelling wave is present. The travelling wavenumber–frequency spectrum is simply the difference of (2.8) and (2.7),

$$S_T(f,\nu) = \widehat{S}(\pm f,\nu) - \tfrac{1}{2}S_S(|f|,\nu). \tag{2.9}$$

The interpretation of positive and negative frequencies is in the direction of propagation. That is, if the data are oriented from west to east, a peak at $(+f_0, \nu_0)$ Hz would imply that the wave is travelling eastward. Note that the travelling spectral estimator can occasionally produce negative estimates and is thus heuristic; see the discussion by Wilks (2011).

The improved statistical properties of the multitaper method can be seen from the expectation (bias) and variance of the estimator. Beginning with bias and assuming unit sampling, we find

$$\boldsymbol{E}\{\widehat{S}(f,\nu)\} = \int_{-1/2}^{1/2}\int_{-1/2}^{1/2} \left(\frac{1}{J}\sum_{j=0}^{J-1} |V^{(j)}(f'-f,\nu'-\nu)|^2 \right) S(f',\nu')\,\mathrm{d}f'\,\mathrm{d}\nu', \tag{2.10}$$

where the bracketed term is called the spectral window and is the Fourier transform pair of our data taper. The convolution of the true spectrum with the spectral window is the source of bias. Ideally the spectral window would be a delta function to yield an unbiased estimator; but from the Paley–Wiener theorem, all non-parametric spectral estimates of this form are biased. The bias is thus controlled by the energy-concentrating properties of the chosen tapers.

As regards estimator variance, note that the use of orthogonal tapers will produce independent spectral estimates. Averaging these estimates produces a reduction in variance that gets larger with the number of tapers used. Multitaper estimators are χ^2_J distributed even when the original data are non-Gaussian distributed (Mallows 1967).

Using the single data taper $v^{(0)}(t,\ s) = 1/\sqrt{N_t N_s}$ in (2.7), one obtains the periodogram estimate, denoted $P(f,\nu)$, of the frequency–wavenumber spectrum. The spectral window for the periodogram is simply the outer product of two Fejér kernels,

$$\mathcal{F}(\nu,f) = \frac{\sin N_s(\nu-\nu')}{N_s\sin(\nu-\nu')}\cdot\frac{\sin N_t(f-f')}{N_t\sin(f-f')}. \tag{2.11}$$

As $\mathcal{F}$ decays relatively slowly away from the origin, this allows far-field frequencies to contribute significantly to local estimates; that is, it admits a large amount of spectral leakage. (Appendix figure 7 shows cross-shaped spectral leakage from 2-D Fejér kernel bias. See, for example, Percival & Walden (1993, figure 200) for a one-dimensional Fejér kernel.) The periodogram ordinates $P(\nu)$ and $P(\nu')$

https://doi.org/10.1017/jfm.2018.366 Published online by Cambridge University Press

are asymptotically independent for Fourier frequencies $\nu' \neq \nu$, and this estimator is asymptotically unbiased. Unfortunately, for finite samples of real data the periodogram is often badly biased, since $\mathcal{F}(\nu, f)$ does not have a large enough range to resolve steep drops in magnitude with frequency or wavenumber. Furthermore, there is no way to bound the bias or quantify the decay of the bias with increasing sample size (Percival & Walden 1993, pp. 197–204). It is also inconsistent, since its variance does not decrease as one increases the sample size. Smoothing of the periodogram is recommended in order to reduce the variance, although this is done at the expense of additional bias.

Careful choice of the set of orthonormal tapers $v^{(j)}(t, s)$ provides two main advantages: (i) The average of J independent spectral estimators has its variance reduced by a factor of nearly $1/J$. Furthermore, by letting the sample size increase in both time and space dimensions, the variance goes to zero, provided that the number of tapers grows with sample size. (ii) The taper $v^{(j)}(t, s)$ will be chosen so that it controls the bias. In this way the multitaper method allows one to control the trade-off between bias and variance of the estimator. In the next section, we describe a family of optimal Cartesian tapers for a prescribed spectral region.

2.2. *Spatiospectral concentration*

In a series of five ground-breaking papers Slepian (1978) described the extent to which a (one-dimensional) discrete sequence can have its power spectrum concentrated on a centred frequency band. The collection of optimally concentrated sequences, described first as the eigenfunctions of a linear integral operator, form an orthonormal set and are computed in practice as the solutions to a tridiagonal matrix eigenvalue problem (Grünbaum 1981). We note that few of these sequences are well concentrated within the designated frequency band and that the number of well-concentrated sequences decreases as the frequency band is contracted (Slepian 1978).

Spatiospectral concentration in higher-dimensional domains has been described by Slepian (1964) and for Cartesian domains by Simons & Wang (2011). In a similar fashion to the univariate formulation, we seek functions supported on the region $\mathcal{R}$ whose Fourier transform has its energy maximally concentrated in a region $\mathcal{K}$. The univariate case described above corresponds to $\mathcal{R}$ and $\mathcal{K}$ being intervals on the real line. Simons *et al.* (2011) show that these functions are given as the eigenfunctions of the linear integral operator

$$(T\varphi)(\boldsymbol{x}) := \int_{\mathcal{R}} D(\boldsymbol{x}, \boldsymbol{x}')\varphi(\boldsymbol{x}')\,\mathrm{d}\boldsymbol{x}', \tag{2.12}$$

where the function D is an integral over our supported region $\mathcal{K}$,

$$D(\boldsymbol{x}, \boldsymbol{x}') = \int_{\mathcal{K}} \mathrm{e}^{\mathrm{i}(\boldsymbol{x}-\boldsymbol{x}')^T\boldsymbol{s}}\,\mathrm{d}\boldsymbol{s}. \tag{2.13}$$

Denote by $\{v^{(j)}\}$ the eigenfunctions of T, ordered by the magnitude of their eigenvalues, few of which are particularly well concentrated as in the univariate case. The corresponding eigenvalues to those eigenfunctions (denoted by v and with Fourier transform pair V) represent the energy concentration in the region $\mathcal{K}$,

$$\lambda_j = \frac{\displaystyle\int_{\mathcal{K}} |V^{(j)}(\boldsymbol{s})|^2\,\mathrm{d}\boldsymbol{s}}{\displaystyle\int_{\mathbb{R}^d} |V^{(j)}(\boldsymbol{s})|^2\,\mathrm{d}\boldsymbol{s}}. \tag{2.14}$$

https://doi.org/10.1017/jfm.2018.366 Published online by Cambridge University Press

When $\mathcal{K}$ is a ball of radius K, the eigenfunctions of T can be found analytically in polar coordinates and expressed by using an expansion in Bessel functions (Simons & Wang 2011, equation (62)). In our application, however, our data are supported on a rectangular grid, and so we compute these functions by using quadrature to solve a corresponding eigenvalue problem. We will refer to the spectral radius as the radius of the spectral region of concentration, analogous to bandwidth in the univariate case. For details on the analytical solution and numerical integration, refer to the work of Simons & Wang (2011).

2.2.1. *Variance estimation, confidence intervals and hypothesis testing for the spectrum*

The eigenspectra $\widehat{S^{(j)}}(f, \nu)$, produced as intermediates of the multitaper computation, are approximately independent and hence can be used to produce an estimate of variance (Thomson 1982). The delete one jackknife method of Efron & Stein (1981), Thomson (1990), Thomson & Chave (1991), Thomson (1994), described here, gives an estimate having less bias than one computed directly as a sample variance of the individual eigenspectra (Cressie 1981) and is statistically efficient for computation on a small number of independent samples. Here we jackknife the logarithms of the spectra for the purpose of stabilizing the estimator (Thomson 1990).

Beginning with the eigenspectra $\widehat{S}^{(j)}(f, \nu)$ from (2.6) for $j = 0, \ldots, J-1$, one computes delete-one estimates of the log spectrum

$$\ln \widehat{S}_{\setminus j}(f, \nu) = \ln \left[\frac{1}{J-1} \sum_{\substack{\ell=0 \\ \ell \neq j}}^{J-1} \widehat{S}^{(\ell)}(f, \nu) \right] \tag{2.15}$$

$$= \ln \left[\frac{1}{J-1} (J\bar{S}(f, \nu) - \widehat{S}^{(j)}(f, \nu)) \right], \tag{2.16}$$

valid for the simple average multitaper estimate (2.7). The average of the delete-one estimates is denoted

$$\ln \widehat{S}_{\setminus \bullet}(f, \nu) = \frac{1}{J} \sum_{j=0}^{J-1} \ln \widehat{S}_{\setminus j}(f, \nu). \tag{2.17}$$

The intermediate quantities can be treated as if they come from a normal sample (Cressie 1981). Thus their variance is t-distributed with $J-1$ degrees of freedom. The resulting variance estimate is

$$\widehat{\sigma}^2(f, \nu) = \frac{(J-1)^2}{J(J-\frac{1}{2})} \sum_{j=0}^{J-1} [\ln \widehat{S}_{\setminus j}(f, \nu) - \ln \widehat{S}_{\setminus \bullet}(f, \nu)]^2. \tag{2.18}$$

We construct the $100(1-\alpha)\,\%$ confidence intervals according to

$$\widehat{S}(f, \nu) \mathrm{e}^{t_{J-1}(\alpha/2)\widehat{\sigma}(f,\nu)} < S(f, \nu) \leqslant \widehat{S}(f, \nu) \mathrm{e}^{t_{J-1}(1-\alpha/2)\widehat{\sigma}(f,\nu)} \tag{2.19}$$

as in the work of Thomson & Chave (1991, equation (2.49)), where t is the Student-t quantile.

https://doi.org/10.1017/jfm.2018.366 Published online by Cambridge University Press

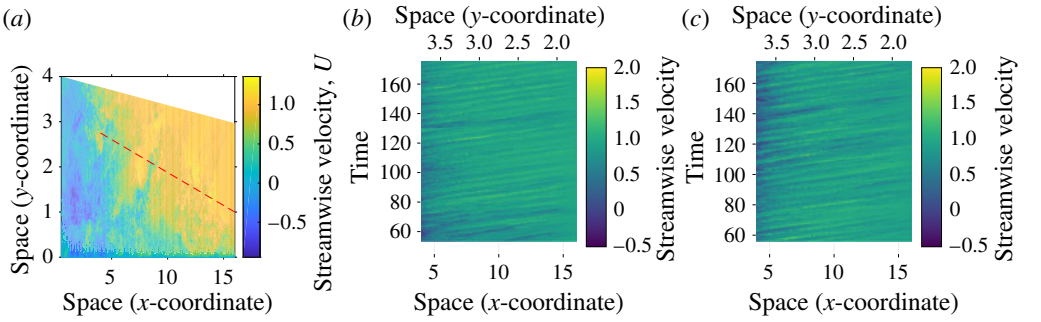


FIGURE 1. (*a*) Shows a still frame of the fluid motion in the wake of the cylinder. The red dotted line shows the spatial extent of the data examined. (*b*) Shows the evolution of the laminar data through time. (*c*) Shows the turbulent data. Lower *x*-axes show the *x*-coordinate, and upper *x*-axes show the (redundant) *y*-coordinate as the data evolve through time.

3. Example: flow around a square wall-mounted cylinder

Vinuesa *et al.* (2015) used direct numerical simulation (DNS) to study the flow around a wall-mounted square cylinder using both turbulent and laminar inflow conditions. The computational domain consisted of a rectangular region having size 24×12 non-dimensional units (d), where a square cylinder with height $4d$ and width d was mounted on the floor at a distance of $8d$ from the upstream inflow, and the fluid was observed for a distance of $16d$ following the obstacle; see Vinuesa *et al.* (2015, figure 1) for a schematic.

The effect of inflow conditions was assessed by considering two different cases with matching momentum-thickness Reynolds numbers $Re_\theta \approx 1000$ at the obstacle: the first case is a fully turbulent zero-pressure-gradient boundary layer, and the second one is a laminar boundary layer with prescribed upstream Blasius inflow profile. A key finding was that the main vortex shedding frequency, determined by power spectral analysis of a time history at the selected point $(7, 4.2, 3)d$, was $St \approx 0.1$ for both inflow conditions, in agreement with earlier studies.

Data were extracted from the centre plane ($z = 0$), where x and y are streamwise and wall-normal coordinates, respectively, and U is streamwise velocity. The domain of interest was in the wake of the cylinder (see figure 1) and was composed of 221 y-direction and 441 x-direction Gauss–Legendre–Lobatto gridpoints. Temporally, the laminar data had a duration of 122 non-dimensional time units and 306 samples for a spacing of $\delta t_L = 0.4000$, while the turbulent data had a duration of 118.644 non-dimensional time units and 724 samples for a spacing of $\delta t_T = 0.1641$.

3.1. *Frequency–wavenumber analysis*

For the present study, data were linearly interpolated to a one-dimensional slice in the $z = 0$ plane having 282 spatial points, illustrated in figure 1. The spacing between points in the x-direction was $0.0427d$ and in the y-direction was $0.0062d$. The endpoints of the line segment were $(4.0, 2.75)d$ and $(16.0, 1.0)d$. This particular choice of domain was chosen as it bisects the opposing vortices that make up the von Kármán vortex street, as determined by visually analysing several frozen panes of flow at various times. Multitaper frequency–wavenumber spectra were computed for both the laminar and turbulent inflow conditions using $K = 9$ and 5 tapers,

https://doi.org/10.1017/jfm.2018.366 Published online by Cambridge University Press

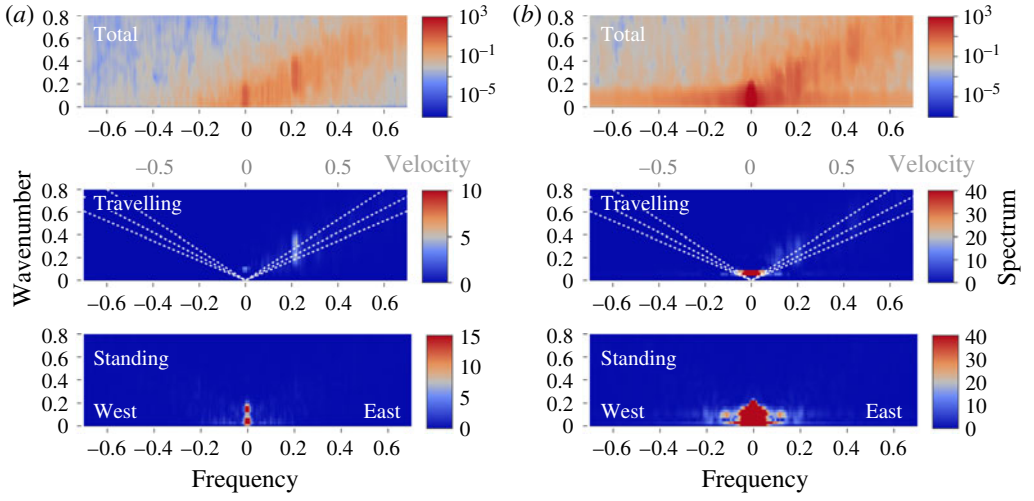


FIGURE 2. Multitaper frequency–wavenumber spectra are shown in the top axes of panels (*a*) and (*b*) with travelling (2.9) (middle) and standing (2.8) (bottom) axes. Travelling spectra are annotated on the upper x-axis with velocities for the travelling waves, the white dotted lines show velocities of $0.75, 0.95, 1.15d$ units per time unit, from closest to y-axis to farthest. Standing spectra are in the bottom axes. Note that the top (logarithmic) colour bar corresponds only to the top axes and the bottom (linear scale) colour bar corresponds to the bottom two (travelling and standing) spectra. (*a*) Shows frequency–wavenumber spectra for the laminar case. (*b*) Shows turbulent spectra computed by using 5 2-D Slepian tapers with $K = 9$. Total laminar spectrum shows a discrete line near $(f, \nu) = (0.2, 0.21)$ indicating a discrete oscillation with velocity $0.95d$/time unit. The turbulent spectrum appears to have no such discrete line frequency.

shown in figure 2. Figure 2(*a*,*b*) shows that standing variation (bottom axes) in both regimes appears to be concentrated mainly near the origin. Middle axes show a large amount of travelling variation, particularly along the line with velocity approximately $0.95d$/time unit (white dashed line). Note also that accumulation of energy is more pronounced at the specific frequency pair (0.2, 0.21) for the laminar flow. The total spectra, defined in (2.7) and shown in the top axes, also show that turbulent-regime flows have power concentrated near zero wavenumber at high frequencies.

Comparing each individual pixel of the total spectrum in the two regimes, being careful to interpolate the turbulent spectrum to the same frequency grid, one obtains figure 3(*a*) which shows the difference between the laminar and turbulent inflow condition spectra in units of standard deviations of the laminar spectrum. In this case, we see that the largest difference between the spectra occurs near the origin and the point (0.2, 0.21). Note that the dominant frequency of 0.2 is in contrast to the $St = 0.1$ obtained by the authors of the original study for a different point in the geometry, outside that plotted in figure 1(*a*). Drawing a straight line through (0, 0) and (0.2, 0.21) and then interpolating the two total spectra along this line results in figure 3(*b*), which shows the laminar and turbulent spectra in green and purple, respectively, with 95 % confidence intervals annotated as semitransparent bands about the spectrum estimate. Turbulent spectra have significantly more low-frequency power through the origin to the onset of the inertial subrange, as is seen from the non-overlapping confidence limits in the $f \in (0, 0.01)$ interval, with little overlap

https://doi.org/10.1017/jfm.2018.366 Published online by Cambridge University Press

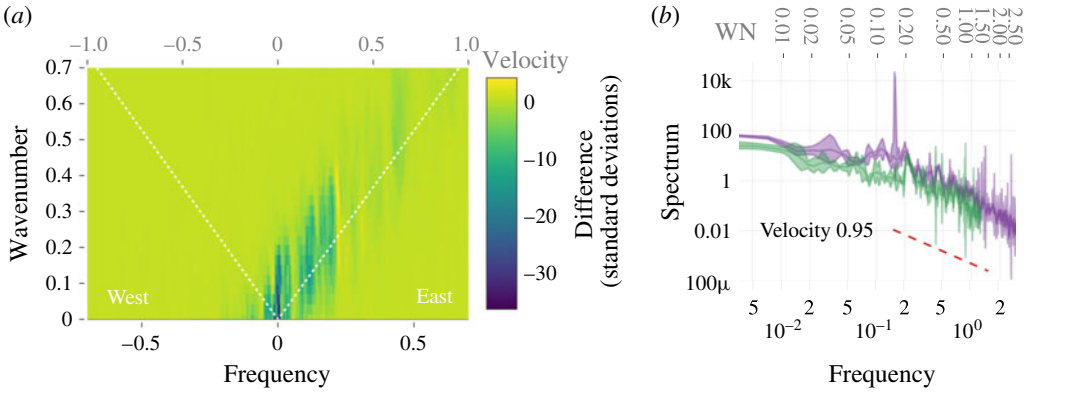


FIGURE 3. (*a*) Shows a pointwise difference of the laminar and turbulent spectra in units of the estimated standard deviation of the laminar spectrum. That is, hot areas show spots where the spectra differ significantly; we see that both near the origin and at the frequency–wavenumber pair $\sim(0.2, 0.21)$ there are differences. (*b*) Shows the interpolated spectra along the line with velocity $0.95d$ per time unit: purple corresponds to turbulent spectrum with 95 % confidence intervals, and green corresponds to laminar spectrum with 95 % confidence intervals. The dashed line is proportional to $f^{-5/3}$, plotted approximately along the inertial subdomain. Additionally, frequency is shown on the lower x-axis, and wavenumber is shown on the upper x-axis.

until $f = 0.2$. There is a discrete line frequency near 0.21 in the laminar inflow case which does not feature as significantly in the turbulent spectrum.

Also annotated in this panel is the $-5/3$ inertial range scaling regime which holds in both wavenumber and frequency. Note that there is no flattening of the spectrum in the higher frequencies which indicates we have not observed the so-called 'noise floor' which is usually introduced by spatial resampling.

To conclude, the present results complement the univariate spectral analysis presented in the work by Vinuesa *et al.* (2015), where here we have found that the second harmonic of the fundamental frequency $St = 0.1$ dominates in the region of the wake we consider. In general, univariate spectral analysis provides an incomplete description of the spatio-temporal flow characteristics, and merely summarizes the aggregate temporal information. Two-dimensional spectral analysis has enabled the quantification and visualization of standing and travelling oscillations in the two inflow scenarios.

3.2. *Comparison of multitaper method with periodograms*

Multitaper spectra in figure 2 have a comparatively large spectral radius, as can be seen in comparison with the periodogram in figure 4. However, the periodograms have a number of features that show its inutility for scientific purposes. For one, the 'railroad track'-shaped artefact near the line $(0, \nu)$ shows that the periodogram window leaks power from near the origin into cross-shaped sidelobes with peaks and troughs of predictable width. Further, the periodograms are overly variable yet are not accompanied by confidence intervals. Finally, periodograms often give very negative estimates for travelling waves. As has been mentioned before, Von Storch and Zweirs point out that this decomposition is merely heuristic and that negative values cannot be taken seriously.

https://doi.org/10.1017/jfm.2018.366 Published online by Cambridge University Press

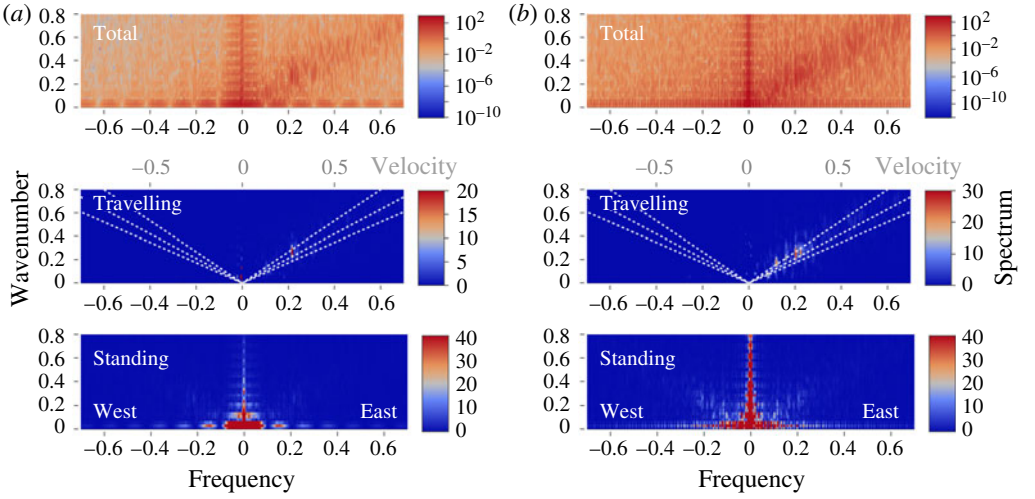


FIGURE 4. Periodogram frequency–wavenumber spectra for (*a*) laminar and (*b*) turbulent inflow cases. The same conventions as figure 2 have been followed.

4. Conclusions

We have introduced a fully spatio-temporal approach to the harmonic and spectral analysis of spatio-temporal flows in one space and one time dimension that additionally allows for the identification of velocities of travelling vortices and for the direct comparison of covariance structures in multiple datasets. The multitaper method we have introduced improves on naïve periodogram estimation by decreasing the bias using concentrated two-dimensional Cartesian tapers, mitigating some of the challenges that have been historically associated with multidimensional spectral density estimation.

Vortex shedding in the wake of a wall-mounted square cylinder was observed in a DNS with both laminar and turbulent inflow conditions. Using univariate spectral analysis on a time history at a single point in the geometry, one finds a single salient vortex shedding frequency ($St \approx 0.1$) in the two regimes. After application of frequency–wavenumber spectral analysis, we find in the laminar case a higher energy concentration at a single frequency–wavenumber pair, corresponding to a strong discrete harmonic oscillation, whereas in the turbulent case we find a $-5/3$ energy cascade along a line having velocity 0.95. Additionally implied by our analysis is that the dominant vortex shedding frequency differs as a harmonic of the fundamental vortex shedding frequency in various regions of the wake.

The strength of the methods introduced here is that they allow for improved quantitative analysis and comparison of the frequency–wavenumber characteristics (standing and travelling wave interpretation) of spatio-temporal flows. In the particular example we give, one can not only determine the properties of these data, but can compare quantitatively the point estimates of the spectral densities using the bootstrapped confidence intervals, which is a useful companion method to those employing estimated optimal bases to study the data like those provided by the POD and DMD.

A number of fluid dynamics applications of this technique are apparent. Although we have demonstrated the utility of this approach for comparing two simulation

https://doi.org/10.1017/jfm.2018.366 Published online by Cambridge University Press

outputs, one could use this technique for verification. Spectra with confidence intervals like those we show here can be computed without carefully matching the sampling properties of both processes, something unlikely to be the case given computational considerations.

Acknowledgements

The authors are grateful to R. Vinuesa and P. Schlatter from the Royal Institute of Technology (KTH), Sweden, and O. Marin from Argonne National Laboratory for providing the DNS data and advice. We also thank D. J. Thomson for advice on the statistical methodology. M.A. acknowledges partial NSF funding through awards FP061151-01-PR and CNS-1545046. This material was based upon work supported by the US Department of Energy, Office of Science, Office of Advanced Scientific Computing Research, under Award DE-SC0008603 and Contract DE-AC02-06CH11347.

Appendix A. A note on preprocessing

It is helpful to demean a time series before computing the spectrum, as the zeroth-frequency bin of the Fourier transform contains the squared sum of the entire series and can be very large relative to the signal variance, which causes a spectral window artefact to be added to the result. In higher dimensions, large power near zero frequency and/or wavenumber may produce an unwanted artefact that has the shape of the spectral window additively introduced at every bin.

Consider that very different results can be obtained by demeaning a process $x(t, s)$ by subtracting a sample mean computed by the following methods.

$$\hat{\mu}^{n}(t, s) = \frac{1}{N_t N_s} \sum_{t=0}^{N_t-1} \sum_{s=0}^{N_s-1} x(t, s), \qquad \text{overall} \tag{A 1}$$

$$\hat{\mu}^{st}(t, s) = \frac{1}{N_t} \sum_{t=0}^{N_t-1} \left[x(t, s) - \frac{1}{N_s} \sum_{s=0}^{N_s-1} x(t, s) \right], \qquad \text{spacetime} \tag{A 2}$$

$$\hat{\mu}^{ts}(t, s) = \frac{1}{N_s} \sum_{s=0}^{N_s-1} \left[x(t, s) - \frac{1}{N_t} \sum_{t=0}^{N_t-1} x(t, s) \right], \qquad \text{timespace.} \tag{A 3}$$

Equation (A 1) has been used to compute figure 3(*a*,*b*). However, the methods above are not advisable as these result in non-zero power on $f = 0$ or $\nu = 0$. Instead we prefer to compute the cosine and sine coefficients $a(t, \nu)$ and $b(t, \nu)$ on the spatially demeaned series, and then demean the cosine and sine coefficients by removal of the temporal sample means.

The result is that the zeroth-frequency bin is small, but the zeroth wavenumber bin may be large. In short, it is important to explain at the outset of the computation how the zero frequency and zero wavenumber components have been removed.

Appendix B. Frequency–wavenumber analysis of a toy dataset

To illustrate the nature of the Hayashi decomposition of a two-dimensional spatio-temporal spectrum into standing and travelling components, we give two short tutorial examples here.

https://doi.org/10.1017/jfm.2018.366 Published online by Cambridge University Press

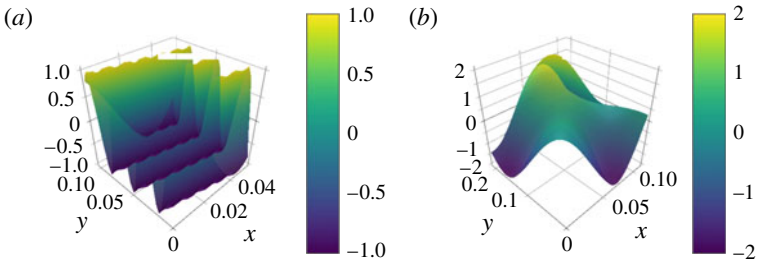


FIGURE 5. (*a*) $Y_{st}(t, s)$ standing and (*b*) $Y_{tr}(t, s)$, travelling waveform, equations (B 1), (B 2). Here we show only a subsection of the data, for clarity.

B.1. *Example*

Consider the following model equation,

$$Y_{st}(t, s) = \cos(2\pi(0.01)t/N_t)\cos(2\pi(0.025)s/N_x) \tag{B 1}$$

$$Y_{tr}(t, s) = \cos(2\pi(0.1)t + 2\pi(0.04)s) \tag{B 2}$$

$$x(t, s) = 2Y_{st}(t, s) + Y_{tr}(t, s) + \zeta(t, s), \tag{B 3}$$

where $\zeta(t, s)$ is a zero-mean white noise process with variance 1. The first process is a standing wave with frequency and wavenumber $(f, \nu) = (0.01, 0.025)$. The second is a travelling wave with frequency and wavenumber $(f, \nu) = (0.1, 0.04)$. We simulate these processes with $N_s = 306$ m spatial samples and $N_t = 282$ s temporal samples, a portion of which is shown in figure 5.

The frequency–wavenumber spectra of the process $x(t, s)$ is shown in figure 6(*a*), periodogram, and 6(*b*), multitaper, where the spatial Fourier coefficients have been de-meaned. The travelling wave produces a pair of antisymmetric peaks in the total frequency–wavenumber diagram with amplitude 1/2. The standing component produces four peaks in the total spectrum with amplitude 1/4. From the travelling wave spectral density, one finds a peak at $(f, \nu) = (0.1, 0.04)$, which corresponds to a wave that travels 10 m in 25 s, so the velocity is 2.5 m s^{-1}, eastward. The travelling wave spectrum in figure 6(*b*) shows, in dotted white, the lines for which the velocities are the same. Annotations on the middle panel of figure 6 show lines having equal velocity at 2.5 m s^{-1}.

B.2. *Example*

A simple standing pattern wave having $N_s = 282$ spatial points and a domain size of 1 spatial unit, and $N_t = 306$ temporal points and 1 temporal unit is generated using the formula

$$x(t, s) = \sigma^2 w(t, s) + \sum_{i=1}^{\ell} A_i \cos(2\pi\phi_i s)\cos(2\pi\psi_i t), \tag{B 4}$$

where $\ell = 2$, $A_1 = 150 = A_2$ and $\phi_1 = 0.2$, $\phi_2 = 0.2$ and $\psi_1 = 0.23$, $\psi_2 = 0.23$ and $w(t, s)$ is unit variance white noise with $\sigma^2 = 1$. Thus, one expects delta function impulses at $(\pm 0.2, \pm 0.2)$ and $(\pm 0.23, \pm 0.23)$ in the spectra. The periodogram and multitaper spectra with $K = 9.0$ and 5 tapers are shown in figure 7. From the periodograms

https://doi.org/10.1017/jfm.2018.366 Published online by Cambridge University Press

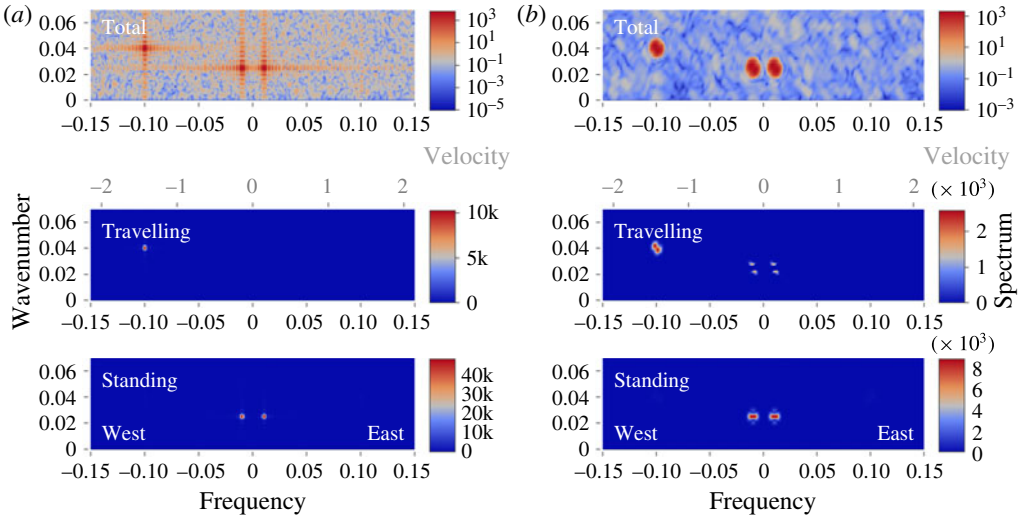


FIGURE 6. (*b*) Shows wavenumber–frequency multitaper spectra of the same data as (*a*) where a periodogram has been computed with additive unit variance white noise (B 3), where $K = 7.0$ and 2 tapers were used. The upper plot shows the total wavenumber–frequency spectrum, the middle plot the travelling wavenumber–frequency spectrum and the bottom plot the standing wavenumber–frequency spectrum. Negative frequencies in this context are to be interpreted as westward, or opposite to streamwise traveling waves. Domain wavenumber is the number of waves that fit in the domain. The travelling wavenumber–frequency spectrum is annotated with a line of equal velocity, from closest to the origin to farthest, velocity equal to 2.5, with grey tick marks in the top of the middle axis annotating the velocities. Total spectrum is on a logarithmic scale, while travelling and standing spectra are on a linear scale, and slightly negative values saturate at zero.

on the left-hand side, one observes large amounts of cross-shaped spectral leakage whose interference produce spurious artefacts. On the right-hand panels, the multitaper spectra in the top panel have much reduced broadband leakage, while maintaining power within a short radius. While the periodogram estimate appears to range over nearly eleven decades, the multitaper estimate ranges over just eight. The reason for this is twofold: multitaper estimators are statistically more stable than periodograms, that is, they have less variance, but when the spectrum truly contains large-power narrowband phenomena, multitaper estimators average that power over a small disk in spectral space, which results in a slight reduction in range.

For further examples, consult von Storch & Zwiers (1999, §§ 11.5.6 and 11.5.11).

Appendix C. A note on visualization of travelling wave spectra

It is important to note that while the expressions for total and standing spectra strictly enforce positivity, the travelling wave spectrum cannot be guaranteed to be positive (von Storch & Zwiers 1999, §§ 11.3.6 and 11.5.11). In some cases this can be simply be caused by statistical fluctuations, but there are also theoretical examples which prescribe negative travelling wave variances. We emphasize that negative values in the travelling wave spectrum have no meaningful interpretation, and that the travelling wave spectrum should only be used to identify places where there is

https://doi.org/10.1017/jfm.2018.366 Published online by Cambridge University Press

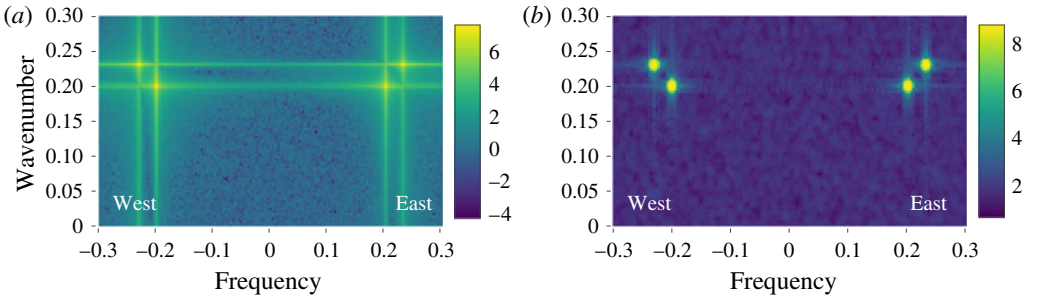


FIGURE 7. (*a*) Shows periodograms, (*b*) shows multitaper (total) spectra with $K = 9.0$ for data generated using (B 4). Note the logarithmic-base 10 colour scale. Closely spaced standing waves produce peaks having strong interference patterns. Due to the energy-concentrating properties of the Cartesian tapers, one achieves less leakage reduction at the expense of larger peak width.

meaningful (positive) energy. On a related note, values for standing wave variance can exceed the total spectrum when the travelling wave point estimates are negative.

When one faithfully reproduces the large negative values that can result in the travelling wave spectrum, plausible features of the travelling wave spectrum become harder to identify and interpret, as the colour scale is skewed by negative estimates that have no meaning. To best visualize the positive, informative part of the travelling wave spectrum, we simply set negative values to zero, and do not modify large values in the standing component.

REFERENCES

BERKOOZ, G., HOLMES, P. & LUMLEY, J. L. 1993 The proper orthogonal decomposition in the analysis of turbulent flows. *Annu. Rev. Fluid Mech.* **25**, 539–575.

CRESSIE, N. 1981 Transformations and the jackknife. *J. Roy. Statist. Soc.* B **43**, 177–182.

CRESSIE, N. & WIKLE, C. K. 2011 *Statistics for Spatio-Temporal Data*. Wiley.

EFRON, B. & STEIN, C. 1981 The jackknife estimate of variance. *Ann. Stat.* **9**, 586–596.

GRÜNBAUM, F. A. 1981 Toeplitz matrices commuting with tridiagonal matrices. *Linear Algebr. Applics.* **40**, 25–36.

HANSSEN, A. 1997 Multidimensional multitaper spectral estimation. *Signal Process.* **58**, 327–332.

HAYASHI, Y. 1979 Space–time spectral analysis of rotary vector series. *J. Atmos. Sci.* **36**, 757–766.

HOLMES, P., LUMLEY, J. L. & BERKOOZ, G. 1998 *Turbulence, Coherent Structures, Dynamical Systems and Symmetry*. Cambridge University Press.

KIRBY, J. F. 2014 Estimation of the effective elastic thickness of the lithosphere using inverse spectral methods: the state of the art. *Tectonophysics* **631**, 87–116.

MALLOWS, C. L. 1967 Linear processes are nearly Gaussian. *J. Appl. Probab.* **4**, 313–329.

PERCIVAL, D. B. & WALDEN, A. T. 1993 *Spectral Analysis for Physical Applications: Multitaper and Conventional Univariate Techniques*. Cambridge University Press.

PRATT, R. W. 1976 The interpretation of space–time spectral quantities. *J. Atmos. Sci.* **33** (6), 1060–1066.

ROWLEY, C. W. 2005 Model reduction for fluids, using balanced proper orthogonal decomposition. *Intl J. Bifurcation Chaos* **15**, 997–1013.

ROWLEY, C. W., MEZIĆ, I., BAGHERI, S., SCHLATTER, P. & HENNINGSON, D. S. 2009 Spectral analysis of nonlinear flows. *J. Fluid Mech.* **641**, 115–127.

https://doi.org/10.1017/jfm.2018.366 Published online by Cambridge University Press

SCHMIDT, O. T., TOWNE, A., COLONIUS, T., CAVALIERI, A. V. G., JORDAN, P. & BRÈS, G. A. 2017 Wavepackets and trapped acoustic modes in a turbulent jet: coherent structure eduction and global stability. *J. Fluid Mech.* **825**, 1153–1181.

SIMONS, F. J. & WANG, D. V. 2011 Spatiospectral concentration in the Cartesian plane. *Intl J. Geomath.* **2** (1), 1–36.

SLEPIAN, D. 1964 Prolate spheroidal wave functions, Fourier analysis and uncertainty IV. *Bell System Tech. J.* **43**, 3009–3057.

SLEPIAN, D. 1978 Prolate spheroidal wave functions, Fourier analysis, and uncertainty V: the discrete case. *Bell System Tech. J.* **57** (5), 1371–1429.

VON STORCH, H. & ZWIERS, F. W. 1999 *Statistical Analysis in Climate Research*. Cambridge University Press.

THOMSON, D. J. 1982 Spectrum estimation and harmonic analysis. *Proc. IEEE* **70** (9), 1055–1096.

THOMSON, D. J. 1990 Quadratic-inverse spectrum estimates: applications to paleoclimatology. *Phil. Trans. R. Soc. Lond.* A **332**, 539–597.

THOMSON, D. J. 1994 An overview of multiple-window and quadratic-inverse spectrum estimation methods. *Proc. ICASSP* **VI**, 185–194; invited plenary lecture.

THOMSON, D. J. & CHAVE, A. D. 1991 Jackknifed error estimates for spectra, coherences, and transfer functions. In *Advances in Spectrum Analysis and Array Processing* (ed. S. Haykin), vol. 1, chap. 2, pp. 58–113. Prentice-Hall.

VINUESA, R., SCHLATTER, P., MALM, J., MAVRIPLIS, C. & HENNINGSON, D. S. 2015 Direct numerical simulation of the flow around a wall-mounted square cylinder under various inflow conditions. *J. Turbul.* **16**, 555–587.

WILKS, D. S. 2011 *Statistical Methods in the Atmospheric Sciences*. Academic Press.

https://doi.org/10.1017/jfm.2018.366 Published online by Cambridge University Press